

Black carbon emissions generally underestimated in the global south as revealed by globally distributed measurements

Received: 13 February 2025

Accepted: 18 July 2025

Published online: 31 July 2025

 Check for updates

A list of authors and their affiliations appears at the end of the paper

Characterizing black carbon (BC) on a fine scale globally is essential for understanding its climate and health impacts. However, sparse BC mass measurements in different parts of the world and coarse model resolution have inhibited evaluation of global BC emission inventories. Here, we apply globally distributed BC mass measurements from the Surface Particulate Matter Network (SPARTAN) and complementary measurement networks to evaluate contemporary BC emission inventories. We use a global chemical transport model (GEOS-Chem) in its high-performance configuration (GCHP) for high-resolution simulations to relate BC emissions to ambient concentrations for comparison with measurements. Here we find that simulations using the Community Emissions Data System (CEDS) emission inventory exhibit skill ($r^2 = 0.73$) in representing variability in SPARTAN measurements across primarily developed regions with low BC concentrations but exhibit pronounced discrepancy ($r^2 = 0.00019$) across high-BC regions in the Global South, underestimating BC by 38%. Alternative inventories (EDGAR, HTAP) yield similar results. These findings motivate renewed attention to the challenging task of characterizing BC emissions from low- and middle-income countries.

Black carbon (BC) is a distinct carbonaceous material from incomplete combustion¹. BC contributes to the radiative forcing of climate by absorbing solar radiation², influencing cloud processes³, and reducing snow albedo after deposition⁴. BC is also associated with adverse health impacts, including increased risk of cardiovascular and respiratory morbidity and mortality^{5,6}, as well as cancer⁷. Accurate estimates of BC emissions are essential to assess its impacts on climate forcing and human health.

BC primarily originates from residential solid fuel combustion, diesel engines, industrial sources, and open burning^{1,8}. Estimates of global anthropogenic BC emissions in bottom-up inventories are challenging due to data limitations, particularly for residential and industrial sectors in low- and middle-income countries (LMICs) (i.e., the Global South)^{9–11}. For example, residential heating and cooking in

emerging economies heavily rely on wood, crop residue, and charcoal combustion. However, tracking their consumption is challenging, and the emission factors (EFs) are highly dependent on burning conditions, which may not represent the inefficiency of combustion conditions¹². In LMICs, local compliance with control technologies is often variable or unknown. Applying default EFs derived from developed regions to these areas introduces significant uncertainties in industrial sectors¹³.

Most prior evaluations of global BC emission inventories have been conducted across developed regions in the northern mid-latitudes due to the paucity of reliable long-term ambient measurements in the Global South^{14–19}. The Surface PARTiculate mATter Network (SPARTAN, <https://www.spartan-network.org/>) is unique in providing a globally consistent BC dataset from sites in densely populated regions, including rapidly changing cities in the Global

✉ e-mail: ren.yuxuan@wustl.edu

South. SPARTAN is designed to provide long-term globally distributed ground-based measurements of particulate matter (PM) composition^{20–24}. Its consistency in BC measurements and comparability of data across globally distributed sites offers the possibility of robust BC evaluation on a global scale.

Global BC simulations using chemical transport models (CTMs) have historically been performed at a coarse resolution of ~ 200 km^{17,25}, which causes artificial dilution within grid cells and limits the ability to capture fine-scale patterns influenced by localized emissions, complex meteorology, and nonlinear interactions²⁶. This mismatch introduces a representativeness bias between grid-averaged model outputs and pointwise measurements of BC concentrations²⁷. Recent advancements in a global open-source community model (GEOS-Chem) in its high-performance configuration (GCHP)²⁸ have enabled global BC simulations at finer resolutions, such as cubed-sphere C360 ($\sim 25 \times 25$ km²) and C720 ($\sim 12 \times 12$ km²)²⁹. This high-resolution modeling capability enables better connections between global emissions and localized pointwise measurements.

This study evaluates BC emissions from widely used emission inventories via modeled concentrations with multi-year measurements from SPARTAN and other available measurements, focusing on the understudied Global South. Our main analyses use the Community Emissions Data System (CEDS) emission inventory³⁰, with sensitivity analyses using the Emissions Database for Global Atmospheric Research (EDGAR) inventory³¹ and the Task Force on Hemispheric Transport of Air Pollution (HTAP) inventory¹⁰ to better understand the consistency of conclusions. We use GCHP to relate BC emissions to ambient concentrations at the fine resolution needed for spatial representativeness (“Methods section”).

Results and discussion

Global spatial distribution of surface BC

Figure 1 shows the global distribution of ambient ground-level BC concentrations from SPARTAN and complementary measurements, compared with a GCHP simulation at C360 (~ 25 km) resolution using

the CEDS emission inventory. The measurements indicate pronounced spatial heterogeneity of global BC concentrations with identified hot-spots in cities in the Indo-Gangetic plains of South Asia, eastern China, Southeast Asia, and sub-Saharan Africa. Supplementary Table S1 summarizes BC concentrations (mean, median, and standard error) measured by Hybrid Integrating Plate/Sphere (HIPS) at each SPARTAN site (“Methods section”). The Dhaka (Bangladesh) and Addis Ababa (Ethiopia) sites have the highest measured mean BC concentrations of $\sim 5 \mu\text{g}/\text{m}^3$, followed by Kanpur (India), Bandung (Indonesia), and Bujumbura (Burundi), with mean BC concentrations around $4 \mu\text{g}/\text{m}^3$. Relatively low BC concentrations are observed at sites in the US, Canada, and Australia (Fajardo, Puerto Rico, US; Halifax, Canada; Sherbrooke, Canada; Pasadena, US; and Melbourne, Australia) with mean BC concentrations less than $0.5 \mu\text{g}/\text{m}^3$. The simulation generally represents the available measurements in North America and Europe with low BC concentrations of less than $1 \mu\text{g}/\text{m}^3$ across most of the US and Canada. The simulation exhibits less skill elsewhere as will be examined further below.

Developed regions of northern midlatitudes and Australia

In developed regions in northern midlatitudes (i.e., the US, Canada, the Republic of Korea, Taiwan, and Israel) and Australia, there is a high degree of consistency ($r^2 = 0.73$) in the relative spatial distribution between simulated BC concentrations and SPARTAN measurements (Fig. 2). The simulated-to-measured ratios across these SPARTAN sites are 1.45 ± 0.29 (mean \pm standard error) with a median of 1.52. Both the ratio and slope exceed unity, primarily reflecting a simulation overestimate in East Asia that may arise from the recent adoption of BC control technologies³². Evaluation of climate models from the Coupled Model Intercomparison Project Phase 6 (CMIP6) also found an overestimation in East Asia¹⁷. In addition to the evaluation based on SPARTAN, we extend the analysis by incorporating measurements from other available sources for evaluation (“Methods” section). We find that consistency exists when comparing simulated BC concentrations with additional complementary measurements from the

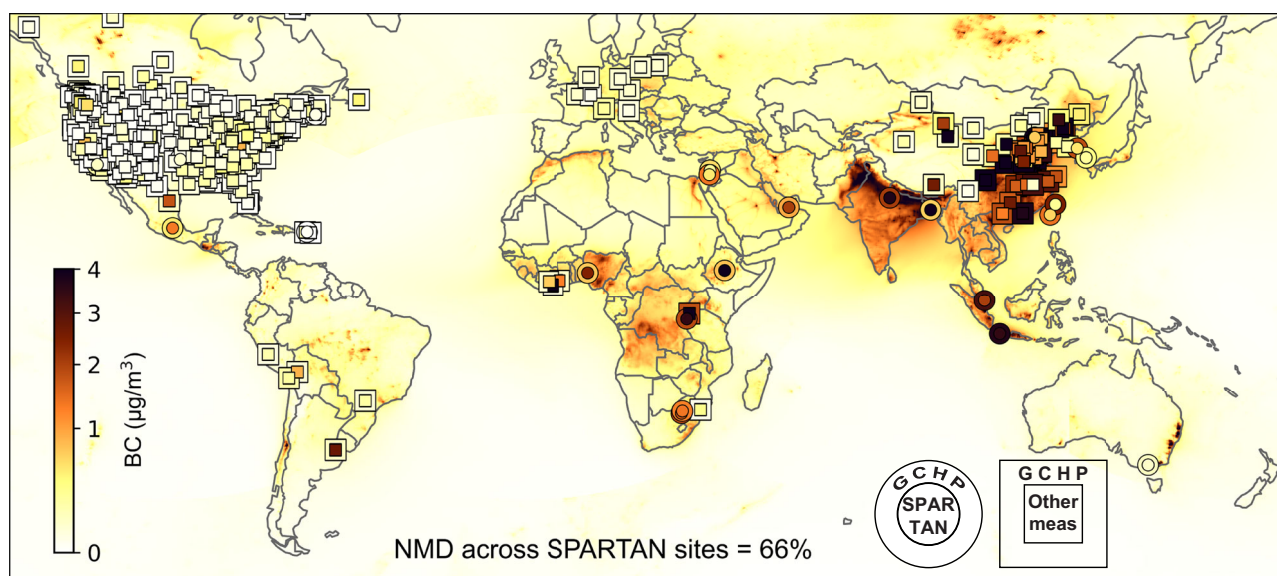


Fig. 1 | Global black carbon (BC) distribution from measurements and simulation using a widely-used emission inventory. This map shows ground-level BC concentrations from SPARTAN measurements over 2019–2023, complementary measurements using original data screening scheme with a six-month sampling length criterion from adjacent years, and a GCHP simulation using the CEDS emission inventory for 2019. SPARTAN and additional measurements are represented by colored circles and squares, respectively, surrounded by concentric circles and squares indicating local coincident GCHP simulated concentrations. The GCHP

simulation is in the background. The inset value is the normalized mean difference (NMD) across SPARTAN sites. Complementary measurements are sourced from the Chemical Speciation Network (CSN) and the Interagency Monitoring of PROtected Visual Environments (IMPROVE) network in the US, the National Air Pollution Surveillance Network (NAPS) in Canada, the European Monitoring and Evaluation Programme (EMEP) in Europe, the China Atmosphere Watch Network (CAWNET)⁶⁴ and Dao et al.⁶⁵ in China; additional data, primarily covering Africa, South America, and South Asia, are referenced from individual studies^{66–72,76–78}.

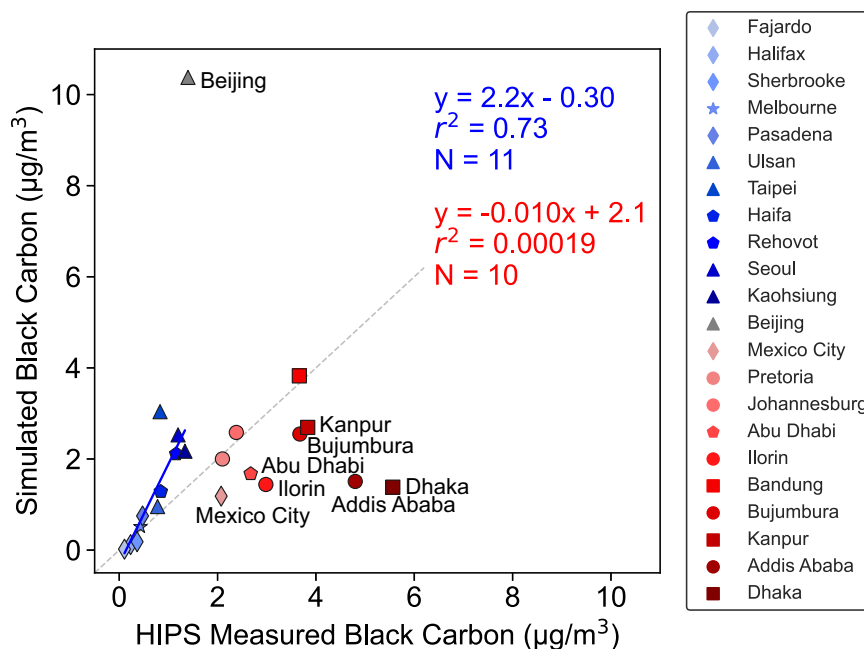


Fig. 2 | Comparison of black carbon (BC) concentrations from SPARTAN measurements and GCHP simulation. Annual mean BC concentrations across SPARTAN sites (2019–2023) are compared with those from the 2019 GCHP simulation. Annotations include the line of best fit (y), coefficient of variation (r^2), and number of comparison points (N). The lowest half of the measured concentrations are

indicated in blue and the upper half in red. The Beijing site, marked in gray, is excluded from statistical calculations due to anomalies in its emissions estimates. Symbols indicate different regions (diamonds for North America, star for Australia, triangles for East Asia, pentagons for the Middle East, circles for Africa, and squares for South Asia).

European Monitoring and Evaluation Programme (EMEP) ($r^2 = 0.93$; slope = 1.2). Other models using widely adopted emission inventories have demonstrated similar skill in developed regions^{14,33}. This consistency reflects the availability of relatively accurate emission data in these areas, which closely represent real-world conditions in these developed regions¹¹.

Discrepancies across the Global South

Despite the model-measurement consistency in developed regions in northern midlatitudes, we find a pronounced discrepancy between simulated BC concentrations and SPARTAN measurements across the Global South ($r^2 = 0.00019$), with underestimates at most sites (Fig. 2). Notably, the average simulated-to-measured ratios are biased low in Dhaka, Bangladesh (0.25), Addis Ababa, Ethiopia (0.31), Ilorin, Nigeria (0.48), Mexico City, Mexico (0.57), Abu Dhabi, the United Arab Emirates (0.63), Bujumbura, Burundi (0.69), and Kanpur, India (0.70). Across 10 Global South sites excluding Beijing, the normalized mean bias (NMB), defined in Supplementary Text S1 of the Supplementary Information, is -38% . The simulated-to-measured ratios across these Global South sites are 0.67 ± 0.09 (mean \pm standard error) with a median of 0.66. Conversely, the simulation exhibits substantial overestimation in Beijing by a factor of 7.4. Evaluation using complementary measurements also suggests a model-measurement discrepancy in the Global South, with additional details discussed in Supplementary Text S2 of the Supplementary Information.

We test how other widely used global anthropogenic emission inventories (i.e., EDGAR v6.1 and HTAP v3) affect the discrepancies in the Global South. Supplementary Fig. S1 compares simulations using EDGAR and HTAP with measurements across SPARTAN sites for 2019. Despite slight differences at individual sites, the comparisons using CEDS, EDGAR, and HTAP in simulations generally exhibit similar results. The simulations remain biased low in most African and Southern Asian sites (e.g., average simulated-to-measured ratios of 0.25, 0.085, and 0.31 in Dhaka for CEDS, EDGAR, and HTAP, respectively) and biased high in Beijing (e.g., average simulated-to-measured

ratios of 7.4, 5.1, and 6.1 for CEDS, EDGAR, and HTAP, respectively). This suggests that the accurate characterization of BC emissions in the Global South is a common challenge across widely used global inventories.

The pronounced discrepancy between simulations and measurements across the Global South is primarily attributed to the difficulty in collecting necessary data for estimating BC emissions. BC emissions in these regions are dominated by diffuse and inefficient combustion sources, including household burning of wood, crop residue, and charcoal, and open trash burning in the absence of refuse collection services and infrastructure^{12,34,35}. The misrepresentation or absence of representing these informal economic activities and the use of dirty fuels have been a persistent challenge in generating BC emission inventories, leading to pronounced underestimates in these regions^{13,36}. For example, in Dhaka, Bangladesh, poorly regulated brick kilns and the burning of agricultural waste, crop residue, fuel wood, and cow dung are major local contributors to BC emissions³⁵. In Addis Ababa, Ethiopia, substantial uncontrolled BC emissions come from heavy-duty diesel vehicles and the widespread use of fuel wood (e.g., eucalyptus) for residential cooking and heating³⁷. Nigeria has an extensive but poorly managed oil and gas exploitation infrastructure, leading to substantial uncontrolled BC emissions due to flaring and illegal oil refining activities^{34,38}. In Burundi, access to reliable electricity is less than 10%³⁹; the inadequate electricity supply and regular power outages lead to dependence on diesel for backup generators and kerosene for lighting in Bujumbura.

In contrast to underestimations found at most sites in the Global South, the simulations substantially overestimate BC concentrations in Beijing (Fig. 2). BC measurements from SPARTAN align with other regional datasets (Supplementary Fig. S2c). Previous studies using the CEDS inventory have also noted model overestimates in Beijing. For example, Ikeda et al.²⁵ evaluated the BC simulation in GEOS-Chem using six widely used emission inventories and found that CEDS reported the highest emissions, overestimating BC in China by a factor of 2.2. China has implemented stringent clean air policies in Beijing,

including the Clean Air Action Plan (2013–2017), the Work Plan for Air Pollution Prevention and Control in Beijing-Tianjin-Hebei (BTH) and Surrounding Areas (2017–2018), and the Action Plan for Blue Sky Defense (2018–2021), leading to a 71% decline in BC concentrations in Beijing from 2012 to 2020⁴⁰. However, these reductions may not be fully captured in the CEDS inventory, which reports only a 35% decrease from 2012 to 2020 and a 2.4% decrease from 2020 to 2022 in total BC emissions across China⁴¹. Moreover, using spatial proxies such as population for emission distributions can introduce anomalies in BC emissions estimates and further contribute to the discrepancies.

Recent advancements in data collection for emission activities and EFs have facilitated efforts to improve BC emission estimates. For example, updates to global BC emission estimates increased them by 32% by incorporating recently available information on residential energy transitions, household stove upgrades, field-measured EFs for residential stoves, differentiated EFs for motor vehicles, and implementation of end-of-pipe mitigation actions in industry³². Similarly, the Dynamics-aerosol-chemistry-cloud interactions in West Africa (DAC-CIWA) inventory inclusion of open solid waste burning and flaring sources with more recent fuel consumption data and EFs increased BC emissions in Africa by 96% in 2015 compared to the regional Diffuse and Inefficient Combustion Emissions for Africa (DICE-Africa) inventory⁴². Despite these improvements, they remain insufficient to reconcile the 2- to 4-fold underestimation in simulations across the Global South identified in this study. Our findings reveal limited accuracy in representing BC across the Global South, highlighting the need for improved characterization of BC emissions and more rigorous monitoring in these regions.

Alternative explanations to the discrepancies in the Global South arising from BC loss through wet deposition, meteorology, measurement protocol, or representativeness bias are unlikely. The similarity in model performance across sites with diverse precipitation and meteorological environments, such as semi-arid locations (e.g., Addis Ababa, Ethiopia) and moist locations (e.g., Dhaka, Bangladesh), indicates that precipitation and meteorology are unlikely explanations. Sensitivity tests with alternative meteorology (NASA GEOS Forward Processing (GEOS-FP) vs Modern-Era Retrospective Analysis for Research and Applications, version 2 (MERRA-2)) indicate high consistency in simulated BC concentrations, with an r^2 of 0.89 for January and July 2019 despite a difference in January that partially reduces the anomaly at Beijing (Supplementary Fig. S3). Additional sensitivity tests with an alternative wet deposition scheme⁴³ also yield similar conclusions, with an r^2 of 1.0 for January and July 2019 (Supplementary Fig. S4). The consistency in measurement protocol across all SPARTAN sites ensures comparability across locations. These conclusions are robust to tests of potential representativeness bias between measurements and simulation, as discussed in Supplementary Text S3 of the Supplementary Information.

Uncertainties

SPARTAN incorporates multiple non-destructive methods to measure BC, including Hybrid Integrating Plate/Sphere (HIPS)⁴⁴, Fourier transform infrared spectrophotometer (FT-IR)^{45,46}, and UV-Visible spectrophotometer⁴⁷ (UV-Vis) (“Methods” section). We find high consistency in BC concentrations determined by these methods (Supplementary Fig. S5), with an $r^2 = 0.82$ for HIPS vs FT-IR and $r^2 = 0.85$ for HIPS vs UV-Vis, providing an indication of the reliability of BC measurements within SPARTAN. The slope of 1.3 in the UV-Vis vs HIPS data suggests that the underestimates of BC emissions in the Global South found here could be 30% larger.

The optical measurements depend on the mass absorption cross section (MAC), which varies with aerosol composition, mixing state, and morphology to estimate BC concentration. SPARTAN uses the widely accepted MAC value of $10 \text{ m}^2/\text{g}$ at 633 nm for HIPS measurements, as recommended by the U.S. Interagency Monitoring of

PROtected Visual Environments (IMPROVE) network^{44,48–50}. However, the use of fixed and varying MAC values across different studies introduces uncertainty and complicates the intercomparison of measurements^{15,51}. Some other studies use MAC values that deviate from the traditional $10 \text{ m}^2/\text{g}$, which are described below and for consistency are adjusted to 633 nm by assuming an inverse wavelength dependence. We summarize recent laboratory and field-measured MAC values across different regions and combustion sources in Supplementary Table S2. For freshly emitted BC, Bond and Bergstrom⁵² suggested a MAC of $6.52 \pm 1.05 \text{ m}^2/\text{g}$, and Liu et al.⁵³ recommended a MAC of $6.95 \pm 0.608 \text{ m}^2/\text{g}$. Once released into the atmosphere, aerosol undergoes processes of condensation, aggregation, and aging, which may cause the MAC value to increase due to coating or decrease due to particle coagulation and aggregate collapse. In developed regions, MAC variation is limited, with absolute values generally close to $10 \text{ m}^2/\text{g}$. Singh et al.⁵⁴ found a stable MAC value of $10.9 \text{ m}^2/\text{g}$ with 11% spatial variability across four Arctic sites, which further aligns within 10% with prior studies at northern mid-latitudes and Arctic sites. Similarly, White et al.⁴⁴ found a coefficient of $10.2 \text{ m}^2/\text{g}$ for $b_{\text{abs}}/M_{\text{EC}}$ across 110 IMPROVE sites in the US. In the Global South, despite the limited number of studies, available data generally report MAC values with an uncertainty range of $7 \text{ m}^2/\text{g}$ to $13 \text{ m}^2/\text{g}$, with MAC values from inefficient combustion sources often reported to be lower than $10 \text{ m}^2/\text{g}$. For example, average MAC values from residential biofuel stoves, diesel trucks, and non-road mobile machinery are reported to be 8.03, 7.25, and 9.99, respectively^{55,56}. These lower MAC values would strengthen our conclusion about underestimates in BC emissions in the Global South as discussed further below.

Given the limited regional variation, we apply the best available MAC value of $10 \text{ m}^2/\text{g}$ and conduct a sensitivity test using an uncertainty range of $7 \text{ m}^2/\text{g}$ to $13 \text{ m}^2/\text{g}$ (Supplementary Fig. S6). In this study, using the traditional MAC of $10 \text{ m}^2/\text{g}$ results in high model-measurement consistency in developed regions ($r^2 = 0.73$; slope = 2.2) but reveals substantial discrepancies across the Global South. Alternatively, applying a MAC of $7 \text{ m}^2/\text{g}$ in SPARTAN would improve the model-measurement slope in developed regions ($r^2 = 0.73$; slope = 1.5) and partially address the model overestimation in Beijing, by reducing the simulated-to-measured ratio from 7.4 to 5.2, but would increase the model-measurement bias in the Global South such as in Dhaka (0.17), Addis Ababa (0.22), Ilorin (0.34), and Mexico City (0.40), thus strengthening the conclusions of this study. Conversely, using a MAC of $13 \text{ m}^2/\text{g}$ would slightly mitigate the pronounced discrepancy in the Global South (e.g., increasing the simulated-to-measured ratio in Dhaka from 0.25 to 0.32). Unrealistic MAC values of $40 \text{ m}^2/\text{g}$ for Dhaka, $32 \text{ m}^2/\text{g}$ for Addis Ababa, and $21 \text{ m}^2/\text{g}$ for Ilorin would be needed to achieve unity simulated-to-measured BC ratios. Thus, despite uncertainties surrounding the exact MAC value, the overall conclusion remains that BC emissions are generally underestimated in the Global South.

We examine the potential effect of COVID-19 lockdowns on our analyses. Exclusion of the period Jan 2020 – Jul 2021 that may have been affected by COVID-19 lockdowns would reduce the total number of samples by 7.8%, and would introduce a NMB versus the full dataset of only -3.2% without affecting our conclusions. Thus we err on the side of inclusion and present the full dataset for completeness.

Dust, in addition to BC, contributes to absorption and can interfere with BC determination in any absorption-based measurement. Among major dust elements, iron (Fe) serves as a tracer for absorbing dust and has a distinct association with absorption^{15,44}, independent of BC. To account for this, we apply a dust correction by subtracting Fe's contribution to absorption and use the adjusted BC concentrations for comparison with simulations (Supplementary Text S4). While this correction leads to a slight decrease in BC concentrations (with a NMB of -9.7%), its impact on emission evaluations is negligible. Consistency remains high for primarily developed regions, while discrepancies

persist across most Global South sites, with r^2 values changing only slightly from 0.71 to 0.74 and 0.00019 to 0.00035, respectively (Supplementary Fig. S7). Although the total Fe content used for correction is an imperfect indicator of absorbing dust, as it includes both (hydr)oxides responsible for absorption and structural Fe in non-absorbing clays, the minimal impact of this correction confirms that dust interference in BC determination is negligible in this study, reinforcing our conclusion that BC emissions are generally underestimated in the Global South.

Implications

Evaluation of global BC emissions requires long-term, globally consistent measurements of ambient BC concentrations, with emissions and concentrations linked through high-resolution simulations for spatial representativeness. We evaluated widely used global emission inventories (CEDS, EDGAR, HTAP) against a dataset of globally distributed SPARTAN measurements using GCHP simulations at the fine resolution of C360 (~25 km). In contrast to the general model-measurement consistency found in primarily developed regions in northern midlatitudes and Australia, we found a pronounced discrepancy between simulated BC concentrations using current emission inventories and ground-based measurements across regions with high BC concentrations in the Global South. BC emissions in the Global South are largely dominated by diffuse and inefficient combustion sources, the misrepresentation or absence of which complicated the generation of accurate BC emission inventories and likely contributed to the discrepancy identified in this study. This highlights the need for renewed efforts to accurately characterize BC emissions in LMICs.

The consistent and substantial underestimation in BC at most Global South sites is of global relevance. The widespread 2- to 4-fold underestimation in BC across sites in Bangladesh, Ethiopia, Nigeria, and Mexico suggests that the radiative effect and health impacts of BC may be larger than previously expected, which highlights the continued importance of BC mitigation efforts with potential co-benefits for both climate and health that warrants further investigation.

Despite SPARTAN's efforts to provide long-term reliable measurements across globally distributed sites, additional geographic coverage in Africa and South America remains desirable. Additionally, variations in instrumentation, sampling objectives, and methodologies among other individual studies create challenges for intercomparison and model evaluation. This highlights the need for expanded measurement networks across additional locations to improve our understanding of BC concentrations and emissions, particularly in the Global South.

Methods

SPARTAN filter measurements and analysis

SPARTAN is a long-term project that measures the ground-based chemical composition of PM at globally dispersed sites in densely populated regions. Overviews of SPARTAN are provided by Snider et al.^{22,23}, Weagle et al.²⁴, McNeill et al.²¹, and Liu et al.²⁰. Supplementary Table S3 provides specific location details for globally distributed SPARTAN sites. High population density and poorly sampled regions are two key factors in site selection. Rooftop placement enhances spatial fetch, better represents urban background, and offers instrument security. The PM_{2.5} is collected on 25 mm Teflon filters (PT25DMCAN-PF03A, Measurement Technology Laboratories) using AirPhoton (Baltimore, MD) SS5 sampling stations at a target flow rate of 5 L/min. The sampling station follows either a standard sampling protocol or the National Aeronautics and Space Administration (NASA) – Italian Space Agency (ASI) Multi-Angle Imager for Aerosols (MAIA) sampling protocol. Under the standard sampling protocol, PM_{2.5} is collected at staggered 3-hour intervals over a 9-day period, generating a 24-hour PM_{2.5} sample covering a full diel cycle. Under the MAIA sampling protocol, PM_{2.5} is collected continuously for 24 h from 9 am

to 9 am at a mission-defined frequency, which has been typically every 3 days during the sampling periods used here.

SPARTAN incorporates multiple techniques to measure BC, including HIPS, FT-IR, and UV-Vis. HIPS determines absorption from the backscattered as well as transmitted and forward-scattered He-Ne laser light (633 nm), with rigorous calibration (Supplementary Text S5) and using a MAC of 10 m²/g as recommended by the IMPROVE network^{44,48–50}. FT-IR collects transmission scans from 4000 cm^{−1} to 420 cm^{−1} in the mid-infrared region and calculates absorbance spectra, which are calibrated to accurately predict thermal optical reflectance (TOR) elemental carbon (EC) measured as part of the IMPROVE network^{45,46}. UV-Vis measures the transmittance and reflectance from 300 to 900 nm at 1 nm resolution and calculates optical depth and MAC for each filter. The BC fraction is determined as the ratio of the calculated MAC to the analytical MAC value of 4.58 m²/g for EC at 900 nm⁴⁷. A potential drawback of the UV-Vis method is the assumption of MAC contribution from BC only at near-IR (>800 nm) wavelengths. Recent studies have shown that strongly absorbing organics, called dark brown carbon, could contribute to enhanced near-IR aerosol absorption^{57,58}. Details on analysis procedures and calibration information for each method can be found in Supplementary Text S5 and White et al.⁴⁴ for HIPS, Dillner and Takahama⁴⁵ and Debus et al.⁴⁶ for FT-IR, and Pandey et al.⁴⁷ for UV-Vis. All these methods are non-destructive, and filters are measured by all three methods according to protocol. This allows for independent measurements of filters and enables intercomparison of BC measurements within SPARTAN. We use the HIPS data for comparison with simulations due to its greater number of measurements and broader usage, and apply the FT-IR and UV-Vis data for intercomparison with HIPS. This study includes 2257 filters from 22 SPARTAN sites with BC measurements between 2019 and 2023⁵⁹. Specific location details for SPARTAN sites are summarized in Supplementary Table S3. The sampling period and number of samples for each site are summarized in Supplementary Table S1.

Emission inventory

We evaluate three widely used global anthropogenic emission inventories (CEDS v2, EDGAR v6.1, and HTAP v3) gridded at 0.1 × 0.1° (~10 km) resolution with monthly seasonality. All three inventories are developed using a bottom-up approach where emissions are estimated using reported activity data (e.g., fuel consumption) and source- and region-specific EFs (i.e., the mass of pollutant emitted per unit of fuel consumed). The CEDS v2 inventory³⁰ provides BC emissions from 1980 to 2019 as a function of anthropogenic sectors (energy generation; industry; transportation; residential, commercial, and other; solvents; agriculture; waste; and shipping) and fuel categories. CEDS scales default emission estimates to align with reliable regional and national inventories, thus producing global emissions that closely reflect contemporary and regionally specific estimates. The EDGAR v6.1 inventory³¹ independently estimates BC emissions from 1970 to 2018 using a globally consistent methodology across all regions, offering sector-specific data with enhanced transparency and comparability. The HTAP v3 inventory¹⁰ provides BC emissions from 2000 to 2018 by integrating six official inventories covering North America, Europe, and parts of Asia (China, India, Japan, and South Korea) with the EDGAR v6.1 for the remaining regions. Sector definitions for CEDS v2, EDGAR v6.1, and HTAP v3 are detailed in Supplementary Table S4.

Despite variations among global inventories, an overall assessment of the 2019 BC emissions indicates that residential, transportation, and industrial sectors are the dominant anthropogenic sources, while energy and waste contribute relatively smaller fractions (Supplementary Fig. S8). The relative contribution of these sectors also exhibits considerable regional variations. For example, the residential sector plays a larger role across South Asia and Sub-Saharan Africa, while transportation accounts for a relatively greater share in North America, North Africa, and the Middle East. In addition to

anthropogenic sources, biomass burning contributes significantly to total BC emissions in Central Sub-Saharan Africa, Tropical and Andean Latin America, and Australasia.

GEOS-Chem simulation

We use GCHP (<http://www.geos-chem.org>), the high-performance configuration of the GEOS-Chem model, that operates with a distributed memory framework for massive parallelization²⁸ to simulate ground-level BC concentrations. GCHP enables the fine resolution needed to interpret global BC measurements. We use GEOS-Chem 13.4.1⁶⁰ which includes developments for improved resolution, performance, and usability²⁹. The simulation is driven by assimilated meteorological data from GEOS-FP (<https://gmao.gsfc.nasa.gov/>) at a resolution of $0.25 \times 0.3125^\circ$ (~ 25 km) with 72 hybrid sigma-pressure vertical levels up to 0.01 hPa. We use the standard full chemistry aerosol-oxidant scheme with the BC simulation as described by Wang et al.⁶¹. Emissions for GEOS-Chem are configured using the Harmonized Emissions Component (HEMCO) module v3.4.0⁶². Global anthropogenic emissions are from the CEDS v2 inventory³⁰ (<https://www.pnnl.gov/projects/ceds/>) at $0.1 \times 0.1^\circ$ (~ 10 km) resolution. Open fire emissions are from the daily Global Fire Emissions Database (GFED) v4.1s⁶³ at $0.25 \times 0.25^\circ$ resolution. The BC simulation covers the entire year of 2019 at a cubed-sphere resolution of C360 (~ 25 km) following a 1-month spin-up.

In addition to CEDS, alternative simulations were conducted using widely used global anthropogenic emission inventories, including EDGAR v6.1 at $0.1 \times 0.1^\circ$ resolution³¹ and HTAP v3 at $0.1 \times 0.1^\circ$ resolution¹⁰. These simulations are conducted at a cubed-sphere resolution of C360 (~ 25 km) for 2019. Additional sensitivity tests include simulations with the highest available resolution of C720 (~ 12 km) using CEDS for January and July 2022, simulations with alternative meteorology (GEOS-FP and MERRA-2) at C180 resolution (~ 50 km) using CEDS for January and July 2019, and simulations with additional wet deposition developments as described by Luo et al.⁴³ at C360 resolution (~ 25 km) using CEDS for January and July 2019.

Other available measurements

We compare measured BC concentrations at globally distributed SPARTAN sites with those reported in regional networks and individual studies. Measurements are sourced from the Chemical Speciation Network (CSN) (2019) (<https://www.epa.gov/amtic/chemical-speciation-network-csn/>) and the IMPROVE network (2019) (<https://vista.cira.colostate.edu/improve/>) in the US, the National Air Pollution Surveillance Network (NAPS) (2019) (<https://data-donnees.az.ec.gc.ca/data/air/monitor/national-air-pollution-surveillance-naps-program/>) in Canada, the EMEP (2019) (<https://www.emep.int/>) in Europe, the China Atmosphere Watch Network (CAWNET)⁶⁴ (2017) and Dao et al.⁶⁵ (2022) in China; additional data, primarily covering Africa, South America, and South Asia, are referenced from individual studies^{66–78} (Supplementary Table S5). To maximize site representativeness, the data are screened to only include ambient measurements from urban, suburban, semi-rural, and rural locations. We prioritize measurements from 2019 to ensure comparability, but we also include data from adjacent years if 2019 data are unavailable. We require measurements to have continuous sampling periods over at least six months and for use in calculating an annual average. To improve regional coverage, we further relax the sampling length criterion to two months for an additional complementary dataset alongside the original. Both datasets are used for model evaluation. Both thermal measurements representing EC and optical measurements representing BC are included.

Data availability

The BC data used in this study have been deposited in the Zenodo repository under accession code <https://doi.org/10.5281/zenodo.15345524>.

The complete BC dataset from SPARTAN is publicly available at <https://www.spartan-network.org/>.

Code availability

GEOS-Chem in its high-performance configuration version 13.4.1 can be downloaded at <https://doi.org/10.5281/zenodo.6564711>. All plots in this manuscript are generated using open-access Python libraries Cartopy (<https://scitools.org.uk/cartopy/>) and Matplotlib (<https://matplotlib.org>).

References

- Bond, T. C. et al. Bounding the role of black carbon in the climate system: a scientific assessment. *J. Geophys. Res. Atmos.* **118**, 5380–5552 (2013).
- Horvath, H. Atmospheric light absorption – a review. *Atmos. Environ.* **27**, 293–317 (1993).
- Koch, D. & Del Genio, A. D. Black carbon semi-direct effects on cloud cover: review and synthesis. *Atmos. Chem. Phys.* **10**, 7685–7696 (2010).
- Hansen, J. & Nazarenko, L. Soot climate forcing via snow and ice albedos. *Proc. Natl Acad. Sci. USA* **101**, 423–428 (2004).
- Geng, F. et al. Differentiating the associations of black carbon and fine particle with daily mortality in a Chinese city. *Environ. Res.* **120**, 27–32 (2013).
- Janssen, N. A. H. et al. Black carbon as an additional indicator of the adverse health effects of airborne particles compared with PM₁₀ and PM_{2.5}. *Environ. Health Perspect.* **119**, 1691–1699 (2011).
- Lequy, E. et al. Contribution of long-term exposure to outdoor black carbon to the carcinogenicity of air pollution: evidence regarding risk of cancer in the Gazel Cohort. *Environ. Health Perspect.* **129**, 037005 (2021).
- Rönkkö, T. et al. Review of black carbon emission factors from different anthropogenic sources. *Environ. Res. Lett.* **18**, 033004 (2023).
- Bond, T. C. et al. A technology-based global inventory of black and organic carbon emissions from combustion. *J. Geophys. Res. Atmos.* **109**, D14203 (2004).
- Crippa, M. et al. The HTAP_v3 emission mosaic: merging regional and global monthly emissions (2000–2018) to support air quality modelling and policies. *Earth Syst. Sci. Data* **15**, 2667–2694 (2023).
- McDuffie, E. E. et al. A global anthropogenic emission inventory of atmospheric pollutants from sector- and fuel-specific sources (1970–2017): an application of the Community Emissions Data System (CEDS). *Earth Syst. Sci. Data* **12**, 3413–3442 (2020).
- Marais, E. A. & Wiedinmyer, C. Air quality impact of diffuse and inefficient combustion emissions in Africa (DICE-Africa). *Environ. Sci. Technol.* **50**, 10739–10745 (2016).
- Kurokawa, J. & Ohara, T. Long-term historical trends in air pollutant emissions in Asia: Regional Emission inventory in ASia (REAS) version 3. *Atmos. Chem. Phys.* **20**, 12761–12793 (2020).
- Vignati, E. et al. Sources of uncertainties in modelling black carbon at the global scale. *Atmos. Chem. Phys.* **10**, 2595–2611 (2010).
- Zhang, Z., Cheng, Y., Liang, L. & Liu, J. The measurement of atmospheric black carbon: a review. *Toxics* **11**, 975 (2023).
- van Donkelaar, A., Martin, R. V., Li, C. & Burnett, R. T. Regional estimates of chemical composition of fine particulate matter using a combined geoscience-statistical method with information from satellites, models, and monitors. *Environ. Sci. Technol.* **53**, 2595–2611 (2019).
- Ikeda, K., Tanimoto, H., Kanaya, Y., Taketani, F. & Matsuki, A. Evaluation of black carbon concentration levels and trends in East Asia from CMIP6 climate models: comparison to long-term observations in Japan and biases due to Chinese emissions. *SOLA* **19**, 239–245 (2023).

18. Shen, W. et al. Evaluating BC aging processes in the Community Atmosphere Model Version 6 (CAM6). *J. Geophys. Res. Atmos.* **128**, e2022JD037427 (2023).
19. Govardhan, G. R., Nanjundiah, R. S., Satheesh, S., Moorthy, K. K. & Takemura, T. Inter-comparison and performance evaluation of chemistry transport models over Indian region. *Atmos. Environ.* **125**, 486–504 (2016).
20. Liu, X. et al. Elemental characterization of ambient particulate matter for a globally distributed monitoring network: methodology and implications. *Environ. Sci. Technol. Air* **1**, 283–293 (2024).
21. McNeill, J. et al. Large global variations in measured airborne metal concentrations driven by anthropogenic sources. *Sci. Rep.* **10**, 21817 (2020).
22. Snider, G. et al. SPARTAN: a global network to evaluate and enhance satellite-based estimates of ground-level particulate matter for global health applications. *Atmos. Meas. Tech.* **8**, 505–521 (2015).
23. Snider, G. et al. Variation in global chemical composition of PM_{2.5}: emerging results from SPARTAN. *Atmos. Chem. Phys.* **16**, 9629–9653 (2016).
24. Weagle, C. L. et al. Global sources of fine particulate matter: interpretation of PM_{2.5} chemical composition observed by SPARTAN using a global chemical transport model. *Environ. Sci. Technol.* **52**, 11670–11681 (2018).
25. Ikeda, K., Tanimoto, H., Kanaya, Y. & Taketani, F. Evaluation of anthropogenic emissions of black carbon from East Asia in six inventories: constraints from model simulations and surface observations on Fukue Island, Japan. *Environ. Sci. Atmos.* **2**, 416–427 (2022).
26. Zhang, D. et al. Advances in simulating the global spatial heterogeneity of air quality and source sector contributions: insights into the Global South. *Environ. Sci. Technol.* **57**, 6955–6964 (2023).
27. Swall, J. L. & Foley, K. M. The impact of spatial correlation and incommensurability on model evaluation. *Atmos. Environ.* **43**, 1204–1217 (2009).
28. Eastham, S. D. et al. GEOS-Chem High Performance (GCHP v11-02c): a next-generation implementation of the GEOS-Chem chemical transport model for massively parallel applications. *Geosci. Model Dev.* **11**, 2941–2953 (2018).
29. Martin, R. V. et al. Improved advection, resolution, performance, and community access in the new generation (version 13) of the high-performance GEOS-Chem global atmospheric chemistry model (GCHP). *Geosci. Model Dev.* **15**, 8731–8748 (2022).
30. Prime, N. et al. Ceds-satmem gridded – bulk emissions. *Zenodo* <https://doi.org/10.5281/zenodo.7958231> (2023).
31. Monforti Ferrario, F. et al. EDGAR v6.1 global air pollutant emissions. European Commission, Joint Research Centre (JRC), <http://data.europa.eu/89h/df521e05-6a3b-461c-965a-b703fb62313e>. (2022).
32. Xu, H. et al. Updated global black carbon emissions from 1960 to 2017: improvements, trends, and drivers. *Environ. Sci. Technol.* **55**, 7869–7879 (2021).
33. Lee, Y. H. et al. Evaluation of preindustrial to present-day black carbon and its albedo forcing from Atmospheric Chemistry and Climate Model Intercomparison Project (ACCMIP). *Atmos. Chem. Phys.* **13**, 2607–2634 (2013).
34. Marais, E. A. et al. Air quality and health impact of future fossil fuel use for electricity generation and transport in Africa. *Environ. Sci. Technol.* **53**, 13524–13534 (2019).
35. Salam, A. et al. Wintertime air quality in megacity Dhaka, Bangladesh strongly affected by influx of black carbon aerosols from regional biomass burning. *Environ. Sci. Technol.* **55**, 12243–12249 (2021).
36. Wiedinmyer, C., Yokelson, R. J. & Gullett, B. K. Global emissions of trace gases, particulate matter, and hazardous air pollutants from open burning of domestic waste. *Environ. Sci. Technol.* **48**, 9523–9530 (2014).
37. Downward, G. S. et al. Occupational exposure to indoor air pollution among bakery workers in Ethiopia; a comparison of electric and biomass cookstoves. *Environ. Pollut.* **233**, 690–697 (2018).
38. Marais, E. A. et al. Anthropogenic emissions in Nigeria and implications for atmospheric ozone pollution: a view from space. *Atmos. Environ.* **99**, 32–40 (2014).
39. World Bank. Data portal: electricity access, <https://data.worldbank.org/indicator/EG.ELC.ACCS.ZS> (2022).
40. Sun, J. et al. Measurement report: long-term changes in black carbon and aerosol optical properties from 2012 to 2020 in Beijing, China. *Atmos. Chem. Phys.* **22**, 561–575 (2022).
41. Hoesly, R. & Smith, S. CEDS v_2024_04_01 release emission data (v_2024_04_01). *Zenodo* <https://doi.org/10.5281/zenodo.10904361> (2024).
42. Keita, S. et al. African anthropogenic emissions inventory for gases and particles from 1990 to 2015. *Earth Syst. Sci. Data* **13**, 3691–3705 (2021).
43. Luo, G., Yu, F. & Moch, J. M. Further improvement of wet process treatments in GEOS-Chem v12.6.0: impact on global distributions of aerosols and aerosol precursors. *Geosci. Model Dev.* **13**, 2879–2903 (2020).
44. White, W. H., Trzepla, K., Hyslop, N. P. & Schichtel, B. A. A critical review of filter transmittance measurements for aerosol light absorption, and calibration for a decade of monitoring on PTFE membranes. *Aerosol Sci. Tech.* **50**, 984–1002 (2016).
45. Dillner, A. M. & Takahama, S. Predicting ambient aerosol thermal-optical reflectance measurements from infrared spectra: elemental carbon. *Atmos. Meas. Tech.* **8**, 4013–4023 (2015).
46. Debus, B. et al. Quantification of major particulate matter species from a single filter type using infrared spectroscopy – application to a large-scale monitoring network. *Atmos. Meas. Tech.* **15**, 2685–2702 (2022).
47. Pandey, A., Shetty, N. J. & Chakrabarty, R. K. Aerosol light absorption from optical measurements of PTFE membrane filter samples: sensitivity analysis of optical depth measures. *Atmos. Meas. Tech.* **12**, 1365–1373 (2019).
48. Malm, W. C., Sisler, J. F., Huffman, D., Eldred, R. A. & Cahill, T. A. Spatial and seasonal trends in particle concentration and optical extinction in the United States. *J. Geophys. Res. Atmos.* **99**, 1347–1370 (1994).
49. Huffman, H. D. Comparison of the light absorption coefficient and carbon measures for remote aerosols: an independent analysis of data from the IMPROVE network. *Atmos. Environ.* **30**, 73–83 (1996).
50. Pitchford, M. et al. Revised algorithm for estimating light extinction from IMPROVE particle speciation data. *J. Air Waste Manag. Assoc.* **57**, 1326–1336 (2007).
51. Gilardoni, S., Vignati, E. & Wilson, J. Using measurements for evaluation of black carbon modeling. *Atmos. Chem. Phys.* **11**, 439–455 (2011).
52. Bond, T. C. & Bergstrom, R. W. Light absorption by carbonaceous particles: an investigative review. *Aerosol Sci. Tech.* **40**, 27–67 (2006).
53. Liu, F. et al. Review of recent literature on the light absorption properties of black carbon: refractive index, mass absorption cross section, and absorption function. *Aerosol Sci. Tech.* **54**, 33–51 (2020).
54. Singh, M. et al. Mass absorption cross section of black carbon for Aethalometer in the Arctic. *Aerosol Sci. Tech.* **58**, 536–553 (2024).
55. Wu, B. et al. Mass absorption cross-section of black carbon from residential biofuel stoves and diesel trucks based on real-world measurements. *Sci. Total Environ.* **784**, 147225 (2021).

56. Wu, B., Wu, Z., Yao, Z., Shen, X. & Cao, X. Refined mass absorption cross-section of black carbon from typical non-road mobile machinery in China based on real-world measurements. *Sci. Total Environ.* **908**, 168579 (2024).
57. Chakrabarty, R. K. et al. Shortwave absorption by wildfire smoke dominated by dark brown carbon. *Nat. Geosci.* **16**, 683–688 (2023).
58. Cheng, Z. et al. Discrepancies between brown carbon light-absorption properties retrieved from online and offline measurements. *Aerosol Sci. Tech.* **55**, 92–103 (2021).
59. Ren, Y. et al. Input data for “Black carbon emissions generally underestimated in the Global South as revealed by globally distributed measurements”. *Zenodo*, <https://doi.org/10.5281/zenodo.15345524> (2025).
60. The International GEOS-Chem User Community. geoschem/GCHP: GCHP 13.4.1 *Zenodo*, <https://doi.org/10.5281/zenodo.6564711> (2022).
61. Wang, X. et al. Exploiting simultaneous observational constraints on mass and absorption to estimate the global direct radiative forcing of black carbon and brown carbon. *Atmos. Chem. Phys.* **14**, 10989–11010 (2014).
62. Lin, H. et al. Harmonized Emissions Component (HEMCO) 3.0 as a versatile emissions component for atmospheric models: application in the GEOS-Chem, NASA GEOS, WRF-GC, CESM2, NOAA GEFS-Aerosol, and NOAA UFS models. *Geosci. Model Dev.* **14**, 5487–5506 (2021).
63. Giglio, L., Randerson, J. T. & van der Werf, G. R. Analysis of daily, monthly, and annual burned area using the fourth generation global fire emissions database (GFED4). *J. Geophys. Res. Biogeosci.* **118**, 317–328 (2013).
64. Guo, B. et al. Long-term variation of black carbon aerosol in China based on revised aethalometer monitoring data. *Atmosphere* **11**, 684 (2020).
65. Dao, X. et al. Significant reduction in atmospheric organic and elemental carbon in PM_{2.5} in 2 + 26 cities in northern China. *Environ. Res.* **211**, 113055 (2022).
66. Resquin, M. D. et al. Local and remote black carbon sources in the Metropolitan Area of Buenos Aires. *Atmos. Environ.* **182**, 105–114 (2018).
67. Targino, A. C., Krecl, P., Oukawa, G. Y. & Mollinedo, E. M. A short climatology of black and brown carbon and their sources at a suburban site impacted by smoke in Brazil. *J. Environ. Sci.* **136**, 498–511 (2024).
68. Mardoñez-Balderrama, V. et al. Atmospheric black carbon in the metropolitan area of La Paz and El Alto, Bolivia: concentration levels and emission sources. *Atmos. Chem. Phys.* **24**, 12055–12077 (2024).
69. Kouassi, A. et al. Measurement of atmospheric black carbon concentration in rural and urban environments: cases of Lamto and Abidjan. *J. Environ. Prot.* **12**, 855–872 (2021).
70. Peralta, O. et al. Atmospheric black carbon concentrations in Mexico. *Atmos. Res.* **230**, 104626 (2019).
71. Villalobos-Puma, E. et al. Atmospheric black carbon observations and its valley-mountain dynamics: eastern cordillera of the central Andes of Peru. *Environ. Pollut.* **355**, 124089 (2024).
72. Liñán-Abanto, R. N. et al. Black carbon in a city of the Atacama Desert before and after the start of the COVID-19 lockdown: ground measurements and MERRA-2 reanalysis. *Remote Sens.* **15**, 4702 (2023).
73. Reyes, F. et al. Impact of biomass burning on air quality in Temuco City, Chile. *Aerosol Air. Qual. Res.* **21**, 210110 (2021).
74. Blanco-Donado, E. P. et al. Source identification and global implications of black carbon. *Geosci. Front.* **13**, 101149 (2022).
75. Xulu, N. A., Piketh, S. J., Feig, G. T., Lack, D. A. & Garland, R. M. Characterizing light-absorbing aerosols in a low-income settlement in South Africa. *Aerosol Air. Qual. Res.* **20**, 1812–1832 (2020).
76. Kalisa, E. & Adams, M. Population-scale COVID-19 curfew effects on urban black carbon concentrations and sources in Kigali, Rwanda. *Urban Clim.* **46**, 101312 (2022).
77. Curto, A. et al. Predictors of personal exposure to black carbon among women in southern semi-rural Mozambique. *Environ. Int.* **131**, 104962 (2019).
78. Djossou, J. et al. Mass concentration, optical depth and carbon composition of particulate matter in the major southern West African cities of Cotonou (Benin) and Abidjan (Cote d’Ivoire). *Atmos. Chem. Phys.* **18**, 6275–6291 (2018).

Acknowledgements

This work was supported by the Clean Air Fund 001591 (RVM), NASA Grant 80NSSC21K0508 (RVM), NOAA Grants NA230AR4310464 (RVM) and NA24NESX432C0001T101(RVM), and NSF Grant 2020673 (RVM), with additional contributions from NASA and the US Agency for International Development via the MAIA project. The work of S.H. and D.J.D. was carried out at the Jet Propulsion Laboratory, California Institute of Technology under a contract with NASA (80NM0018D0004). P.C.L. is partly supported by the National Health Research Institutes (NHRI-EX114-11410PI). We are grateful to the dynamic team of numerous SPARTAN site operators for their meticulous sample collection. We thank Emily Stone, Crystal L. Weagle, and Brenna Walsh for helping to establish the original SPARTAN protocols. We thank Wenyu Liu, Ryan Graham, Wilson Hou, Zilin Wei, Maya Arnott, Kyla Fung, Manasi Pawar, Michelle Kaibara, Maya Mehrotra, Guinter Vogg, and Emma Walter for contributing to the laboratory analyses of collected samples.

Author contributions

Y.X.R. designed the study, analyzed the data, and wrote the initial manuscript draft. R.V.M. secured funding, co-designed the study, edited the manuscript, and provided guidance throughout the analysis. C.R.O., X.L., H.Z., and E.J.L.R. assisted with the sample collection and data processing within SPARTAN. D.Z. performed GCHP simulations. A.M.D. assisted with HIPS and FT-IR analysis. W.H.W. assisted with HIPS analysis. R.K.C., J.I.K., V.V., and K.S. assisted UV-Vis analysis. S.H., D.J.D., C.A., O.A., A.A., R.Y.C., D.F., P.G., R.M.G., M.G., J.H.K., K.L., P.C.L., P.L., O.L.M., M.N., N.N., N.O., S.S.P., A.S., B.S., Y.S., R.S., S.N.T., E.W., M.T.W., Q.Z., Y.N.R., and M.B. contributed to network establishment, sample collection, instrument maintenance, and coordination at globally distributed SPARTAN sites. All authors read and approved the final manuscript.

Competing interests

The authors declare no competing interests.

Additional information

Supplementary information The online version contains supplementary material available at <https://doi.org/10.1038/s41467-025-62468-5>.

Correspondence and requests for materials should be addressed to Yuxuan Ren.






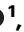









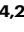

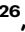
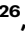

Peer review information *Nature Communications* thanks Yutaka Kondo, who co-reviewed with Sho OhataEgide Kalisa and Rafael Liñán-Abanto for their contribution to the peer review of this work. A peer review file is available.

Reprints and permissions information is available at <http://www.nature.com/reprints>

Publisher’s note Springer Nature remains neutral with regard to jurisdictional claims in published maps and institutional affiliations.

Open Access This article is licensed under a Creative Commons Attribution-NonCommercial-NoDerivatives 4.0 International License, which permits any non-commercial use, sharing, distribution and reproduction in any medium or format, as long as you give appropriate credit to the original author(s) and the source, provide a link to the Creative Commons licence, and indicate if you modified the licensed material. You do not have permission under this licence to share adapted material derived from this article or parts of it. The images or other third party material in this article are included in the article's Creative Commons licence, unless indicated otherwise in a credit line to the material. If material is not included in the article's Creative Commons licence and your intended use is not permitted by statutory regulation or exceeds the permitted use, you will need to obtain permission directly from the copyright holder. To view a copy of this licence, visit <http://creativecommons.org/licenses/by-nc-nd/4.0/>.

© The Author(s) 2025

Yuxuan Ren ¹✉, **Christopher R. Oxford** ¹, **Dandan Zhang** ¹, **Xuan Liu**^{1,2}, **Haihui Zhu** ^{1,3}, **Ann M. Dillner** ⁴, **Warren H. White**⁴, **Rajan K. Chakrabarty** ¹, **Sina Hasheminassab**⁵, **David J. Diner**⁵, **Emmie J. Le Roy** ¹, **Joshin Kumar** ¹, **Valerie Viteri**¹, **Keyao Song**¹, **Clement Akoshile**⁶, **Omar Amador-Muñoz**⁷, **Araya Asfaw**⁸, **Rachel Ying-Wen Chang**⁹, **Diana Francis** ¹⁰, **Paterne Gahungu** ¹¹, **Rebecca M. Garland** ^{12,13}, **Michel Grutter** ⁷, **Jhoon Kim** ¹⁴, **Kristy Langerman** ¹⁵, **Pei-Chen Lee**¹⁶, **Puji Lestari**¹⁷, **Olga L. Mayol-Bracero**¹⁸, **Mogesh Naidoo**¹², **Narendra Nelli** ¹⁰, **Norm O'Neill**¹⁹, **Sang Seo Park**²⁰, **Abdus Salam** ²¹, **Bighnaraj Sarangi**¹⁸, **Yoav Schechner** ²², **Robyn Schofield** ²³, **Sachchida N. Tripathi** ^{24,25}, **Eli Windwer** ²⁶, **Ming-Tsang Wu** ^{27,28}, **Qiang Zhang** ²⁹, **Yinon Rudich** ²⁶, **Michael Brauer** ³⁰ & **Randall V. Martin** ¹

¹Department of Energy, Environmental & Chemical Engineering, Washington University in St. Louis, St. Louis, MO, USA. ²Scripps Institution of Oceanography, University of California San Diego, San Diego, CA, USA. ³Department of Atmospheric Science, Colorado State University, Fort Collins, CO, USA. ⁴Air Quality Research Center, University of California Davis, Davis, CA, USA. ⁵Jet Propulsion Laboratory, California Institute of Technology, Pasadena, CA, USA.

⁶Department of Physics, University of Ilorin, Ilorin, Nigeria. ⁷Instituto de Ciencias de la Atmósfera y Cambio Climático, Universidad Nacional Autónoma de México, Mexico City, Mexico. ⁸Institute of Geophysics and Space Science, Addis Ababa University, Addis Ababa, Ethiopia. ⁹Department of Physics and Atmospheric Science, Dalhousie University, Halifax, NS, Canada. ¹⁰Environmental and Geophysical Sciences Lab, Earth Science Department, Khalifa University, Abu Dhabi, United Arab Emirates. ¹¹Institute of Applied Statistics, University of Burundi, Bujumbura, Burundi. ¹²Council for Scientific and Industrial Research, Pretoria, South Africa. ¹³Department of Geography, Geo-Informatics and Meteorology, University of Pretoria, Pretoria, South Africa. ¹⁴Department of Atmospheric Sciences, Yonsei University, Seoul, Republic of Korea. ¹⁵Department of Geography, Environmental Management and Energy Studies, University of Johannesburg, Johannesburg, South Africa. ¹⁶Department of Public Health, National Cheng Kung University, Tainan, Taiwan. ¹⁷Faculty of Civil and Environmental Engineering, Bandung Institute of Technology, Bandung, Indonesia. ¹⁸Department of Environmental Science, University of Puerto Rico, Puerto Rico, PR, USA. ¹⁹Départ de géomatique appliquée, Université de Sherbrooke, Sherbrooke, QC, Canada. ²⁰Department of Urban and Environmental Engineering, Ulsan National Institute of Science and Technology, Ulsan, Republic of Korea. ²¹Department of Chemistry, University of Dhaka, Dhaka, Bangladesh. ²²Department of Electrical Engineering, Technion Israel Institute of Technology, Haifa, Israel. ²³School of Geography, Earth and Atmospheric Sciences, University of Melbourne, Melbourne, VIC, Australia. ²⁴Department of Civil Engineering, Indian Institute of Technology Kanpur, Kanpur, India. ²⁵Department of Sustainable Energy Engineering, Indian Institute of Technology Kanpur, Kanpur, India. ²⁶Department of Earth and Planetary Sciences, Weizmann Institute of Science, Rehovot, Israel. ²⁷Department of Family Medicine, Kaohsiung Medical University Hospital, Kaohsiung Medical University, Kaohsiung, Taiwan. ²⁸PhD Program in Environmental and Occupational Medicine, Kaohsiung Medical University, Kaohsiung, Taiwan. ²⁹School of Environment, Tsinghua University, Beijing, China. ³⁰School of Population and Public Health, University of British Columbia, Vancouver, BC, Canada. ✉e-mail: ren.yuxuan@wustl.edu